Rubem P. Mondaini *Editor*

Trends in Biomathematics: Exploring Epidemics, Eco-Epidemiological Systems, and Optimal Control Strategies

Selected Works from the BIOMAT Consortium Lectures, Rio de Janeiro, Brazil, 2023

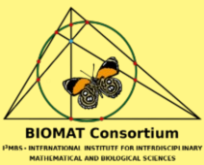

Springer

Trends in Biomathematics: Exploring Epidemics, Eco-Epidemiological Systems, and Optimal Control Strategies

Rubem P. Mondaini
Editor

Trends in Biomathematics: Exploring Epidemics, Eco-Epidemiological Systems, and Optimal Control Strategies

Selected Works from the BIOMAT Consortium Lectures, Rio de Janeiro, Brazil, 2023

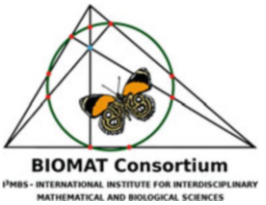

Springer

Editor
Rubem P. Mondaini
BIOMAT Consortium
International Institute for Interdisciplinary
Mathematical and Biological Sciences
Rio de Janeiro, Brazil

Federal University of Rio de Janeiro
Rio de Janeiro, Brazil

ISBN 978-3-031-59071-9 ISBN 978-3-031-59072-6 (eBook)
https://doi.org/10.1007/978-3-031-59072-6

Mathematics Subject Classification: 92Bxx, 92-08, 92-10

This Springer imprint is published by the registered company Springer Nature Switzerland AG
The registered company address is: Gewerbestrasse 11, 6330 Cham, Switzerland

Preface

Over the past four years, the conferences in the BIOMAT international series have had to adapt to the restrictions imposed on international conferences in an online format. Restrictions that proved even more severe for fully interdisciplinary conferences, such as our international symposia.

We often saw the participation of researchers and their students split into groups due to the existence of time zones. Were it not for the professionalism of the colleagues we know so well, it would have been even more difficult, sometimes impossible, to count on the participation of the vast majority, a fundamental condition for maintaining the top level of an interdisciplinary and multidisciplinary conference.

Very scarce financial resources made it impossible to organise hybrid sessions, with some support for PhD students and recent PhDs from developing countries. At all the conferences over the last four years, we have communicated to colleagues during the annual general meetings of our scientific association the decision to continue the mission of jointly organising this series of symposia. We are extremely grateful to all our colleagues. So many years of collaboration have created bonds of admiration and respect between us all.

This year, 2024, we hope to be able to organise our BIOMAT Symposium in person. Negotiations are underway to this end with the directors of the proposing institution. We will keep everyone informed and hope to continue counting on the support that the BIOMAT Consortium has always received.

The BIOMAT 2023 Symposium was held from November 6–9, 2023, and once again we had the support of the RNP/Brazil network and the cooperation of Dr. Beatriz Zoss, to whom we are once again very grateful on behalf of the BIOMAT Consortium. Our collaborators at the organisation's headquarters in Rio de Janeiro, Simão C. de Albuquerque Neto and Carmem Lucia S.C. Mondaini, provided invaluable help.

Rio de Janeiro, Brazil
November 10, 2023

Rubem P. Mondaini

Editorial Board of the BIOMAT Consortium

Contents

Mathematical Modeling of the Vaporization of Encapsulated Perfluorocarbon Nanodroplets Using Chirp Ultrasound: A Review

Kaiwen Jiang, Maryam Ghasemi, and Sivabal Sivaloganathan

Abstract This paper explores the transformative potential of acoustic droplet vaporization (ADV) in biomedical imaging. Emphasizing simulation results from a mathematical model, we investigate the ADV of nanodroplets encapsulated in hyperelastic shells under frequency-modulated ultrasound. Our focus lies on the stability of these phase-change contrast agents (PCCAs) in the bloodstream and the heightened axial resolution achieved with frequency-modulated ultrasound.

Detailing the principles of ultrasound, we underscore its significance in medical imaging and its ability to penetrate soft tissue for comprehensive organ and blood flow analysis. Recognizing challenges in visualizing tissue microvasculature, we highlight limitations of current contrast agents and position ADV as a groundbreaking approach. As a phase-change contrast agent, ADV employs liquid nanodroplets with a carefully chosen boiling point, promising both stability in circulation and enhanced contrast at the imaging site.

This review consolidates insights into the advancements and potential optimizations of ADV under frequency-modulated ultrasound, presenting it as a pivotal development for contrast-enhanced ultrasound imaging. Through a synthesis of preclinical studies, we emphasize the comparable contrast enhancement properties of vaporized nanodroplets to traditional microbubble agents. In summary, this paper offers a comprehensive review of the current state and future prospects of ADV, showcasing its role in advancing contrast-enhanced ultrasound imaging.

K. Jiang · M. Ghasemi
University of Waterloo, Waterloo, ON, Canada
e-mail: k27jiang@uwaterloo.ca; m23ghasemi@uwaterloo.ca

S. Sivaloganathan (✉)
Center for Mathematical Medicine, The Fields Institute, Toronto, ON, Canada
e-mail: ssivalog@uwaterloo.ca

R. P. Mondaini (ed.), *Trends in Biomathematics: Exploring Epidemics, Eco-Epidemiological Systems, and Optimal Control Strategies*,
https://doi.org/10.1007/978-3-031-59072-6_1

1 Introduction

Acoustic droplet vaporization (ADV) is the use of ultrasound waves to induce the vaporization of nanometer-scale droplets through the negative pressure during the rarefaction parts of the ultrasound wave. This can be exploited for biomedical applications such as contrast-enhanced ultrasound imaging, targeted drug delivery, and embolotherapy. In this paper, we present the simulation results of a mathematical model of the ADV of a nanodroplet encapsulated in a hyperelastic shell under frequency-modulated ultrasound—a process that explores the potential of nanodroplets as phase-change contrast agents for ultrasound imaging with improved stability in the bloodstream, together with the enhanced axial resolution of frequency-modulated ultrasound.

1.1 Ultrasound Imaging

Ultrasound is defined as a mechanical sound wave at a frequency beyond the human audible frequency range (>20 kHz). It is generated through the excitation of an ultrasonic transducer (usually based on a piezoelectric or an electromagnetic transducer) [38, 43]. This excitation causes the propagation of longitudinal waves through the imaging medium. When an ultrasound wave encounters materials with differing resistances to ultrasound wave propagation (known as *acoustic impedance*), the difference in acoustic impedance causes a portion of the incident wave energy to be reflected back toward the transducer. The ultrasound wave can also undergo refraction at the interface between two materials with differing speeds of sound. It may also scatter off very small objects in its path, resulting in small amounts of wave energy being distributed in all directions. Reflected or scattered waves may eventually return to the transducer where they are then detected. The time of flight of the signal from origination to detection, together with the strength of the received signal, can be used to construct an ultrasound image.

For most imaging applications, instead of a continuous signal, pulses of ultrasound consisting of a few wave cycles are emitted which are separated by a specified pulse repetition interval. This allows for reflected or backscattered waves returning to the transducer to be detected as transducers are unable to transmit and receive at the same time.

Ultrasound waves can penetrate soft tissue at depths above 10 cm [33] and can be used to noninvasively provide information on the anatomy and function of internal organs or on blood flow. It has become one of the most commonly performed diagnostic tests today [18].

1.2 Contrast-Enhanced Ultrasound Imaging

Conventional ultrasound imaging techniques encounter difficulty when imaging tissue microvasculature due to the small size of the microvessels and the poor resolution of signal between the blood and the surrounding tissue [6]. This can be improved with the use of contrast agents administered as part of the imaging process that can provide better contrast. As of 2017, three ultrasound contrast agents have been approved by the FDA for clinical applications, all of which come in the form of micrometer-scale bubbles of an inert gas encapsulated by a shell. Lumason® utilizes a phospholipid shell with a sulfur hexafluoride core, Luminity® uses a phospholipid shell with an octafluoropropane core, and Optison® uses an albumin shell with an octafluoropropane core [3].

Alternative contrast agents based on inert liquid perfluorocarbon cores have also been investigated. While their higher molecular weight confers them an increased stability in circulation compared to microbubble-based contrast agents [19, 22], their contrast enhancement effect is less pronounced than their gaseous counterparts [11, 29]. Acoustic droplet vaporization provides a possible best of both worlds solution in the form of phase-change contrast agents (PCCAs). These are liquid nanodroplets with a liquid core specifically chosen to have a boiling point close to human body temperature such that they remain in liquid form in the circulation but are able to vaporize to form microbubbles under the action of ultrasound at the imaging site. Thus, this could provide both the high echogenicity of microbubble contrast agents and the increased stability of inert liquid emulsions. Preclinical studies have suggested that once vaporized, their contrast enhancement properties are comparable to those of microbubble contrast agents [14, 34–36, 42].

1.3 Coded Excitation

The axial resolution of ultrasound imaging is dependent on its spatial pulse length—a product of the number of cycles per pulse and the ultrasound wavelength [9]. Tissue boundaries at distances smaller than half the spatial pulse length cannot be resolved since their reflected signals will overlap.

Reducing the number of cycles in each pulse lowers the total power transmitted and results in a reduced signal-to-noise ratio of the returning signal. Increasing the ultrasound frequency reduces the penetrative depth of ultrasound, since higher-frequency ultrasound undergoes higher attenuation—the absorption of ultrasound into tissues where it is converted into heat and dissipated, together with scattering or internal reflections [27]. At higher frequencies, tissues are unable to keep up with the rapid fluctuations in pressure and are thus unable to transmit as much of the incident wave energy [13], resulting in higher attenuation.

Coded excitation through frequency or phase modulation of the ultrasound waveform can be used to increase axial resolution without sacrificing transmitted

power and penetration depth. An example of a simple coding scheme is a linear chirp (**C**ompressed **Hi**gh-**R**esolution **P**ulse) where the frequency of the ultrasound signal increases linearly from the beginning to the end of the pulse. Other coding schemes such as nonlinear chirps or binary codes also exist [5]. Since the form of the transmitted signal $s(t)$ is known, the received signal can be passed through a matched filter (the time-reversed version of the transmitted signal $s(-t)$) to extract the spatial scattering information within without suffering a loss of resolution arising from using a longer pulse [5].

The first proposed application of coded excitation in medical ultrasound was by Takeuchi in 1979 using phase modulation and Golay codes [40]. Chirp-coded excitation was used for the first time by O'Donnell [24] in B-mode ultrasound imaging to demonstrate the enhanced penetrating power of coded excitation signals. This study also contained a theoretical analysis concluding that a theoretical 15–20 decibel improvement in signal-to-noise ratio over conventional pulsed ultrasound can be obtained using coded excitation. Pedersen et al. modified a commercial ultrasound scanner and used it to demonstrate that chirp-coded ultrasound yielded significantly increased penetration depths and image quality in vivo [28].

2 Mathematical Modeling

An early model of the behavior of encapsulated bubbles was proposed by de Jong et al. where the encapsulating albumin shell contributed an additional loss term due to internal friction within the shell and an additional restoring force due to its stiffness [7]. Guédra and Coulouvrat modeled the encapsulating shell as a viscoelastic Kelvin-Voigt material and found that the acoustic droplet vaporization threshold increases with shell rigidity [10]. The linear elasticity of the Kelvin-Voigt model was limited in its ability to model large shell deformations, which typically resulted in a fivefold increase in the radius of the vapor-droplet system [41]; hence, a modification was made by Lacour using a hyperelastic Mooney-Rivlin shell model instead [16]. Ghasemi et al. later introduced real gas behavior to the perfluoropentane (PFP) vapor within the bubble, where the previous above-described models assumed ideal gas behavior [8].

We present here the results obtained from simulations of encapsulated system devised by Guédra, Coulouvrat, and Lacour, with the real gas behavior incorporated by Ghasemi, under the influence of chirp ultrasound. Particular attention is paid to the derivation of the hyperelastic shell response, as details are scant in the literature.

2.1 Evolution of Bubble Radius over Time

As shown in the schematic in Fig. 1, the model represents the radius of the vapor bubble, the inner and outer radius of the shell as three concentric spheres with radii

Fig. 1 Bubble schematic

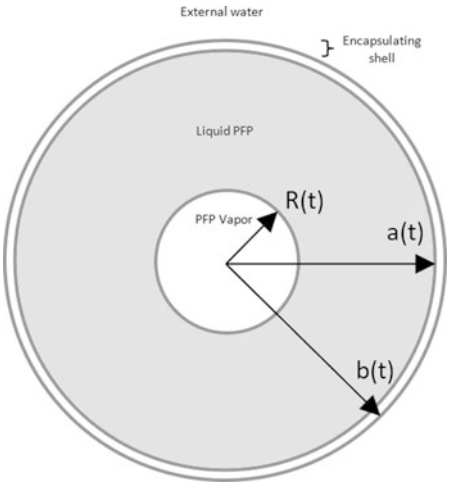

$R(t), a(t), b(t)$, respectively. It is assumed that the space within the inner vapor bubble, between the vapor bubble and the shell, and outside of the shell contains PFP vapor, liquid PFP, and water, respectively. To model the evolution of these values over time, the following dynamics were taken into account:

- Vapor behavior within the bubble
- Mass flux and heat transfer across the bubble surface
- Heat transfer across the three mediums within the system (inner fluid, shell, external fluid)
- Elastic response of the shell
- Viscous fluid flow within the inner and external fluids and the viscous response of the shell

The evolution of the bubble radius over time is described by the generalized Rayleigh-Plesset equation [16] which is obtained as follows. Its derivation begins with the momentum equation of an incompressible continuum with radial symmetry [17, 31].[1] For $r \in (R, \infty)$,

$$\rho\left(\frac{\partial u}{\partial t} + u\frac{\partial u}{\partial r}\right) = \frac{1}{r^2}\frac{\partial}{\partial r}(r^2 T_{rr}) - \frac{T_{\theta\theta} + T_{\phi\phi}}{r}, \tag{1}$$

where ρ is the density, $u := u(r, t)$ is the radial velocity at radial distance r from the bubble center at time t, and $\mathbf{T}$ is the Cauchy stress tensor with $T_{rr}, T_{\theta\theta}, T_{\phi\phi}$ being its components in each direction. By the conservation of mass, for $r \in (R, \infty)$, the radial velocity u must satisfy

[1] Note that [31] uses a different convention where the trace of the stress tensor is separated out as $-\frac{\partial p}{\partial r}$.

$$u(r,t) = \left(\frac{R}{r}\right)^2 U(t), \tag{2}$$

where $U(t) := \lim_{r \to R^+} u(r,t)$ is the velocity of the inner liquid right at the surface of the bubble. We additionally introduce the hydrostatic pressure $p := -\frac{1}{3}\mathrm{tr}(\mathbf{T}) = -\frac{T_{rr}+T_{\phi\phi}+T_{\theta\theta}}{3}$ which is associated with volume change.

From here onward, the subscripts V, L, S, E will be used to denote properties corresponding to the vapor within the bubble, inner liquid, shell, and external liquid, respectively. The continuity of normal stress across each interface (bubble surface, shell inner surface, shell outer surface) gives the following [4, 10, 30]:

$$\begin{aligned}
p(R^+) &= p(R^-) - 4\eta_L \frac{U}{R} - 2\frac{\sigma}{R} + J^2(\rho_V^{-1} - \rho_L^{-1}),\\
p(a^-) &= p(a^+) - T^e_{rr,S}(a) + 4(\eta_S - \eta_L)\left(\frac{R^2 U}{a^3}\right) + 2\frac{\sigma_1}{a},\\
p(b^+) &= p(b^-) - T^e_{rr,S}(b) + 4(\eta_S - \eta_E)\left(\frac{R^2 U}{b^3}\right) - 2\frac{\sigma_2}{b},
\end{aligned} \tag{3}$$

where J is the mass flux across the bubble surface, $U_V := \lim_{r \to R^-} u(r,t)$ is the gas velocity at the inner surface of the bubble, η is the dynamic viscosity of the medium denoted by its subscript, and $\sigma, \sigma_1, \sigma_2$ are the surface tensions corresponding to the bubble surface, shell inner surface, and shell outer surface, respectively.

We introduce the following notation:

$$\begin{aligned}
\Gamma_i &= \rho_L + (\rho_S - \rho_L)\left(\frac{R}{a}\right)^i + (\rho_E - \rho_S)\left(\frac{R}{b}\right)^i,\\
\bar{\sigma} &= \sigma + \sigma_1\left(\frac{R}{a}\right) + \sigma_2\left(\frac{R}{b}\right),\\
\bar{\eta} &= \eta_L + (\eta_S - \eta_L)\left(\frac{R}{a}\right)^3 + (\eta_E - \eta_S)\left(\frac{R}{b}\right)^3,\\
p_V &\coloneqq p(R^-),\\
\Phi &\coloneqq J^2(\rho_V^{-1} - \rho_L^{-1}),\\
\mathcal{S} &\coloneqq \int_a^b 3\frac{T^e_{rr,S} + p}{r} dr,\\
\xi &= \frac{U}{\dot{R}}.
\end{aligned} \tag{4}$$

Integrating Equation 1 from R to ∞ and applying the continuity of normal stress conditions listed above thus results in the general Rayleigh-Plesset equation as stated in [16]:

$$R\dot{U} + \frac{4\xi - \frac{\Gamma_4}{\Gamma_1}\xi^2}{2}\dot{R}^2 = \frac{p_V - \frac{2\bar{\sigma}+4\bar{\eta}U}{R} + \Phi + \mathcal{S} - p_\infty}{\Gamma_1}. \tag{5}$$

In the case of a regular sinusoidal ultrasound pulse, p_∞, the pressure at infinity arising from a constant frequency ultrasound wave is given as follows:

$$p_\infty(t) = p_0 - p_a \sin(2\pi f_0 t), \tag{6}$$

where p_0 is the ambient pressure, p_a is the amplitude of the acoustic wave, and f_0 is the acoustic frequency. For a linear chirp signal, the frequency term increases or decreases linearly between an initial frequency f_0 and a final frequency f_1 over the duration of the pulse T, resulting in

$$p_\infty(t) = p_0 - p_a \sin\left(2\pi\left(f_0 + ct\right)t\right), \tag{7}$$

where

$$c = \frac{f_1 - f_0}{T}. \tag{8}$$

The differential equations describing the evolution of R, a, b over time are as follows:

$$\dot{R} = U - \frac{J}{\rho_L}, \tag{9}$$

$$\dot{a} = \frac{R^2}{a^2}U, \tag{10}$$

$$\dot{b} = \frac{R^2}{b^2}U. \tag{11}$$

The vapor pressure within the bubble p_V, mass flux Φ, and elastic response of the shell $\mathcal{S}$ will be explained in the subsequent sections.

2.2 Vapor Pressure Within the Bubble

On the right-hand side of Equation 5, the vapor pressure within the bubble p_V is obtained using the van der Waals equation [39]:

$$
\begin{aligned}
p_V &= \frac{\rho_V R_g T_b}{1 - b\rho_V} - a\rho_V^2, \\
a &= \frac{27}{64}\frac{R_g^2 T_c^2}{\rho_c}, \\
b &= \frac{R_g T_c}{8 p_c}.
\end{aligned}
\tag{12}
$$

where R_g is the specific gas constant of PFP which is in turn the ratio between the ideal gas constant and the molar mass of PFP, $T_b = T_b(t)$ is the bubble surface temperature, and (T_c, p_c) is the critical point of PFP, which is a pair of temperature and pressure values beyond which superfluidity is observed. The constants a and b correct for the intermolecular forces of attraction and the volume occupied by the gas molecules, both of which are not taken into account in the ideal gas model [39].

Beyond the critical point, superfluidity is observed, in which case the pressure is given by [23]

$$
\begin{aligned}
p_V &= p_c \left(\frac{T_b}{T_c}\right)^{\frac{\gamma_{PT}}{\gamma_{PT}-1}}, \\
\gamma_{PT} &= \left(1 - \frac{\gamma - 1}{\gamma}\frac{R_g T_b - a\rho_V(1-\rho_V)}{R_g T_b - 2a\rho_V(1-\rho_V)^2}\right)^{-1},
\end{aligned}
\tag{13}
$$

where $\gamma = \frac{C_p}{C_v}$ is the ratio of the specific heat at constant pressure to the specific heat at constant volume of PFP.

2.3 Mass Flux and Temperature

In order to determine the pressure contribution due to mass flux Φ as given in Equation 4, the mass flux J is required. It can be obtained by invoking the conservation of energy at the bubble interface [12]:

$$
K_L \left.\frac{\partial T}{\partial r}\right|_{r \to R^+} - K_V \left.\frac{\partial T}{\partial r}\right|_{r \to R^-} = LJ, \tag{14}
$$

where $T = T(r, t)$ is the temperature field; K_L and K_V are the thermal conductivities of the liquid PFP and PFP vapor, respectively; and L is the latent heat of vaporization of PFP. The heat conduction within the bubble can be neglected due to the large difference between the thermal conductivity and diffusivity coefficients of the liquid and vapor phases, allowing us to assume that the temperature distribution is uniform within the bubble [10, 12]. Therefore, $\left.\frac{\partial T}{\partial r}\right|_{r \to R^-} = 0$ and

$$J = \frac{K_L}{L}\frac{\partial T}{\partial r}\bigg|_{r \to R^+}. \tag{15}$$

Note that J in the above equation is the negative of what was given in Equation (12) in [10] where they assumed the opposite convention that a positive J corresponds to the mass leaving the bubble into the surrounding liquid PFP droplet. In order to obtain J from the above equation, the temperature profile within the liquid PFP droplet near the bubble surface is required, which entails modeling both the bubble surface temperature $T_b(t)$ and the entire temperature profile $T(r, t)$ over time.

2.4 Bubble Surface Temperature

The modeling of the bubble surface temperature requires the determination of the gas velocity field within the bubble. The enthalpy equation is as follows [32]:

$$\rho_V C_p \frac{\partial T}{\partial t} - \frac{\partial p}{\partial t} = \nabla \cdot (K_V \nabla T). \tag{16}$$

The gas velocity field within the bubble $\mathbf{v}$ is introduced through the continuity equation:

$$\frac{\partial \rho_V}{\partial t} + \rho_V \nabla \cdot \mathbf{v} + \nabla \rho_V \cdot \mathbf{v} = 0. \tag{17}$$

The following property is also used:

$$C_p \rho_V T = \frac{\gamma p}{\gamma - 1}. \tag{18}$$

The Clausius-Clapeyron relation stated below relates the vapor pressure with the temperature:

$$p_V(T) = p_{\text{ref}} \exp\left[\frac{L}{R_g}\left(\frac{1}{T_{\text{ref}}} - \frac{1}{T}\right)\right], \tag{19}$$

where p_{ref} and T_{ref} are known values along the vapor pressure-temperature curve. This can be differentiated to obtain the rate of change of pressure over time in terms of the rate of temperature change over time.

Combining Equations 16, 17, and 18 and applying the assumption of radial symmetry, the following is obtained:

$$\frac{\partial(r^2 v)}{\partial r} = \frac{r^2}{\gamma p}\left[\frac{\gamma - 1}{r^2} K_V \frac{\partial}{\partial r}\left(r^2 \frac{\partial T}{\partial r}\right) - \dot{p}\right], \tag{20}$$

where v is the radial velocity of the gas within the bubble. This is integrated to obtain the vapor velocity field. After applying the assumption that the temperature field within the bubble is spatially uniform [10] and combining with the conservation of mass and the Clausius-Clapeyron relation, we can obtain the final differential equation governing the evolution of bubble surface temperature over time:

$$\frac{L}{R_g T_b^2}\frac{dT_b}{dt} = \frac{3\gamma}{R}\left(\frac{K_L}{\rho_V L}\frac{\partial T}{\partial r}\bigg|_{r\to R^+} - \dot{R}\right). \tag{21}$$

The evolution of the gas density ρ_V over time can be obtained by invoking the conservation of mass to be as follows:

$$\frac{d\rho_V}{dt} = \frac{3}{R}(J - \rho_V \dot{R}). \tag{22}$$

2.5 Temperature Within the Inner and Outer Liquids

The temperature profiles within the inner and outer liquids are given by the energy equations [10, 17]:

$$\frac{\partial T}{\partial t} + u(r,t)\frac{\partial T}{\partial r} = \frac{K_m}{\rho_m c_m}\frac{1}{r^2}\frac{\partial}{\partial r}\left(r^2 \frac{\partial T}{\partial r}\right) + \frac{12\eta_m}{\rho_m c_m}\left(\frac{u(r,t)}{r}\right)^2, \tag{23}$$

where $m \in \{L, E\}$ represents the medium for which the temperature profile is being evaluated. The heat flux is assumed to be continuous across the shell:

$$K_L \frac{\partial T}{\partial r}\bigg|_{r\to a^-} = K_E \frac{\partial T}{\partial r}\bigg|_{r\to b^+}. \tag{24}$$

And the other boundary conditions are given by the temperature of the bubble surface and the temperature at infinity, which is held constant:

$$\lim_{r\to R^+} T(r,t) = T_b(t), \tag{25}$$

$$\lim_{r\to\infty} T(r,t) = T_\infty. \tag{26}$$

2.6 Shell Elastic Response

The elastic response of the shell S is given as follows [16]:

$$\mathcal{S} = 3 \int_a^b \frac{T^e_{rr,S} + p}{r} dr \ , \tag{27}$$

within which the elastic stress of the shell can be obtained through first characterizing its deformation and subsequently relating it to the stress through constitutive relations.

2.6.1 Deformation Gradient

Let $P \in \mathbb{R}^3$ be a point with curvilinear coordinates (q_1, q_2, q_3) and position vector $\mathbf{r}$ from the origin. A set of natural basis vectors $\{\mathbf{v}_i \mid i = 1, 2, 3\}$ arise which can be obtained through differentiating the position vector with respect to each coordinate [37]:

$$\mathbf{v}_i = \frac{\partial \mathbf{r}}{\partial q_i}; i = 1, 2, 3. \ , \tag{28}$$

The characterization of an object's deformation requires the specification of two states—the set of points occupied by the object at a selected reference time point (which we can define to be $t = 0$), which will be referred to as the **reference configuration**, and the set of points currently occupied by the object, which will be referred to as the **current configuration**.

The reference configuration is denoted by $\mathcal{R}_0$, and a point P within it with coordinates (Q^1, Q^2, Q^3) can be represented by a position vector in tensor notation $\mathbf{X} = X^i \mathbf{G}_i(\mathbf{X})$, where $\{\mathbf{G}_i(\mathbf{X}) \mid i = 1, 2, 3\}$ is the set of natural basis vectors in the reference configuration at position $\mathbf{X}$.

The motion and deformation of the object causes the point $\mathbf{X}$ to move along a path over time, denoted $\boldsymbol{\chi}_t(\mathbf{X})$, eventually arriving at a point within the current configuration $\mathcal{R}_t$. This is denoted by p with coordinates (q^1, q^2, q^3) and can be represented by a coordinate vector $\mathbf{x} = x^i \mathbf{g}_i(\mathbf{x})$, where $\{\mathbf{g}_i(\mathbf{x}) \mid i = 1, 2, 3\}$ is the set of basis vectors used to describe the current configuration at $\mathbf{x}$. Note that we use the convention that points, coordinates, and vectors in the reference configuration are denoted using capital letters, while their counterparts in the current configuration are denoted using small letters. The dependence of the basis vectors $\mathbf{G}^i$ and $\mathbf{g}^i$ on $\mathbf{X}$ and $\mathbf{x}$ will be omitted in the following text for clarity:

$$\boldsymbol{\chi}_t(\mathbf{X}) = \mathbf{x}. \ , \tag{29}$$

The different sets of basis vectors used in the reference and current configurations provide the generality necessary to describe the problem using curvilinear coordinate systems (e.g., spherical polar coordinates, as is the case here) which vary in space (and thus time as each point moves due to the deformation of the object).

Problems within continuum mechanics can often be solved by relating the current configuration of the object in question back to its reference configuration. This is done by examining the **deformation gradient** (denoted **F**) which uses the gradient of $\chi_t(\mathbf{X}) = \mathbf{x}$ with respect to $\mathbf{X}$ to describe how points within the current configuration change with respect to points within the reference configuration. Its definition and derivation according to [20] is presented as follows:

$$\operatorname{Grad} \mathbf{x} \coloneqq \frac{\partial \mathbf{x}}{\partial Q^i} \otimes \mathbf{G}^i, \tag{30}$$

where $\{\mathbf{G}^i \mid i = 1, 2, 3\}$ is the dual basis of $\{\mathbf{G}_i\}$ defined through the following relation:

$$\mathbf{G}^i \cdot \mathbf{G}_j = \delta^i_j. \tag{31}$$

The deformation gradient is known as a two-point tensor since it has one leg in the reference configuration and another in the current configuration. Expressing $\mathbf{x}$ as a linear combination of the basis vectors, Equation 30 can be expanded as follows:

$$\begin{aligned}
\frac{\partial \mathbf{x}}{\partial Q^i} \otimes \mathbf{G}^i &= \frac{\partial (x^j \mathbf{g}_j)}{\partial Q^i} \otimes \mathbf{G}^i \\
&= \frac{\partial x^j}{\partial Q^i} \mathbf{g}_j \otimes \mathbf{G}^i + x^j \frac{\partial \mathbf{g}_j}{\partial Q^i} \otimes \mathbf{G}^i \\
&= \frac{\partial x^j}{\partial Q^i} \mathbf{g}_j \otimes \mathbf{G}^i + x^j \frac{\partial \mathbf{g}_j}{\partial q^m} \frac{\partial q^m}{\partial Q^i} \otimes \mathbf{G}^i \\
&= \frac{\partial x^j}{\partial Q^i} \mathbf{g}_j \otimes \mathbf{G}^i + x^j \Gamma^k_{jm} \mathbf{g}_k \frac{\partial q^m}{\partial Q^i} \otimes \mathbf{G}^i \\
&= \left(\frac{\partial x^j}{\partial Q^i} + x^k \Gamma^j_{km} \frac{\partial q^m}{\partial Q^i} \right) \mathbf{g}_j \otimes \mathbf{G}^i,
\end{aligned} \tag{32}$$

where Γ^j_{km} are Christoffel symbols that are defined by the following relation for a set of basis vectors $\{\mathbf{g}_i\}$:

$$\Gamma^j_{km} = \mathbf{g}^j \frac{\partial \mathbf{g}_k}{\partial x^m}. \tag{33}$$

We can represent points in the reference and current configurations using spherical coordinates and denote them as $(Q^1, Q^2, Q^3) = (R, \Phi, \Theta)$ and $(q^1, q^2, q^3) = (r, \phi, \theta)$, respectively. Given a point P in the reference configuration with positional vector $\mathbf{X} = \begin{bmatrix} R\sin\Theta\cos\Phi \\ R\sin\Theta\sin\Phi \\ R\cos\Theta \end{bmatrix}$, it can be differentiated with respect to each of the coordinate variables to obtain the natural basis, and Equation 31 can be used to obtain the dual set:

$$\begin{aligned} \mathbf{G}^1(\mathbf{X}) &= \begin{bmatrix} \sin\Theta\cos\Phi \\ \sin\Theta\sin\Phi \\ \cos\Theta \end{bmatrix}, \\ \mathbf{G}^2(\mathbf{X}) &= \begin{bmatrix} -\frac{1}{R\sin\Theta}\sin\Phi \\ \frac{1}{R\sin\Theta}\cos\Phi \\ 0 \end{bmatrix}, \\ \mathbf{G}^3(\mathbf{X}) &= \begin{bmatrix} \frac{1}{R}\cos\Theta\cos\Phi \\ \frac{1}{R}\cos\Theta\sin\Phi \\ -\frac{1}{R}\sin\Theta \end{bmatrix}. \end{aligned} \tag{34}$$

Similarly, a point p in the current configuration with positional vector $\mathbf{x} = \begin{bmatrix} r\sin\theta\cos\phi \\ r\sin\theta\sin\phi \\ r\cos\theta \end{bmatrix}$ admits the following natural basis:

$$\begin{aligned} \mathbf{g}_1(\mathbf{x}) &= \begin{bmatrix} \sin\theta\cos\phi \\ \sin\theta\sin\phi \\ \cos\theta \end{bmatrix}, \\ \mathbf{g}_2(\mathbf{x}) &= \begin{bmatrix} -r\sin\theta\sin\phi \\ r\sin\theta\cos\phi \\ 0 \end{bmatrix}, \\ \mathbf{g}_3(\mathbf{x}) &= \begin{bmatrix} r\cos\theta\cos\phi \\ r\cos\theta\sin\phi \\ -r\sin\theta \end{bmatrix}. \end{aligned} \tag{35}$$

We note that these basis vectors are not normal and can be expressed as a product of their lengths and the corresponding normalized basis vectors $\{\mathbf{E}_R, \mathbf{E}_\Phi, \mathbf{E}_\Theta\}$, $\{\mathbf{e}_r, \mathbf{e}_\phi, \mathbf{e}_\theta\}$:

$$
\begin{aligned}
\mathbf{G}^1(\mathbf{X}) &= \mathbf{E}_R, \\
\mathbf{G}^2(\mathbf{X}) &= \frac{1}{R\sin\Theta}\mathbf{E}_\Phi, \\
\mathbf{G}^3(\mathbf{X}) &= \frac{1}{R}\mathbf{E}_\Theta, \\
\mathbf{g}_1(\mathbf{x}) &= \mathbf{e}_r, \\
\mathbf{g}_2(\mathbf{x}) &= r\sin\theta\mathbf{e}_\phi, \\
\mathbf{g}_3(\mathbf{x}) &= r\mathbf{e}_\theta.
\end{aligned}
\tag{36}
$$

The Christoffel symbols can then be obtained by differentiating the basis vectors $\{\mathbf{g}_1, \mathbf{g}_2, \mathbf{g}_3\}$ with respect to the coordinates and expressing the results as linear combinations of themselves:

$$
\begin{aligned}
\Gamma^2_{12} &= \Gamma^3_{13} = \frac{1}{r}, \\
\Gamma^1_{22} &= -r\sin^2\theta, \\
\Gamma^3_{22} &= -\sin\theta\cos\theta, \\
\Gamma^2_{23} &= \cot\theta, \\
\Gamma^1_{33} &= -r.
\end{aligned}
\tag{37}
$$

For a shell whose points in the reference configuration are given by $\{\mathbf{X} = r_0\mathbf{E}_R \mid r_0 \in [a_0, b_0]\}$ that undergoes the motion and deformation represented by $\boldsymbol{\chi}$ to arrive at its current configuration $\{\mathbf{x} = r(r_0, t)\mathbf{e}_r \mid r \in [a(t), b(t)]\}$, its deformation gradient can be obtained by plugging Equations 36 and 37 into Equation 32 to obtain

$$
\mathbf{F} = \begin{bmatrix} \frac{\partial r}{\partial r_0} & 0 & 0 \\ 0 & \frac{r}{r_0} & 0 \\ 0 & 0 & \frac{r}{r_0} \end{bmatrix}. \tag{38}
$$

To illustrate how the deformation gradient is useful in the characterization of deformations, we shall examine how the deformation affects line and volume elements. Let $d\mathbf{X}$ be an infinitesimal line segment in the direction of $\mathbf{X}$ in the reference configuration. If we denote its length as $dS \coloneqq \|d\mathbf{X}\|$, then it can be expressed as

$$
d\mathbf{X} = \mathbf{M}dS. \tag{39}
$$

where $\mathbf{M}$ is the unit vector in the direction of $\mathbf{X}$. The deformation will cause the infinitesimal line element to transform into $d\mathbf{x}$, with length $ds \coloneqq \|d\mathbf{x}\|$. Let $\mathbf{m}$ be the unit vector in its direction:

$$d\mathbf{x} = \mathbf{m}ds. \tag{40}$$

Now,

$$\mathbf{m} = \mathbf{F}(\mathbf{M}dS) = \mathbf{F}d\mathbf{X}. \tag{41}$$

Now consider a volume element with sides $d\mathbf{X_1}, d\mathbf{X_2}, d\mathbf{X_3}$ in the reference configuration. This has volume

$$dV = d\mathbf{X}_3 \cdot (d\mathbf{X}_1 \times d\mathbf{X}_2). \tag{42}$$

Similarly, the post-deformation volume element with sides $d\mathbf{x_1}, d\mathbf{x_2}, d\mathbf{x_3}$ in the current configuration will have a volume of

$$dv = d\mathbf{x}_3 \cdot (d\mathbf{x}_1 \times d\mathbf{x}_2). \tag{43}$$

Taking the ratio, and applying Equation 41 to each of the sides,

$$\begin{aligned} \frac{dv}{dV} &= \frac{d\mathbf{X}_3 \cdot (d\mathbf{X}_1 \times d\mathbf{X}_2)}{d\mathbf{x}_3 \cdot (d\mathbf{x}_1 \times d\mathbf{x}_2)} \\ &= \det \mathbf{F}. \end{aligned} \tag{44}$$

If an object is incompressible, the volume of any portion of itself must be preserved under deformation, and hence it must satisfy $\det \mathbf{F} = 1$, and applying this restriction to Equation 38 results in

$$\frac{\partial r}{\partial r_0} = \left(\frac{r_0}{r}\right)^2. \tag{45}$$

The deformation gradient can thus be expressed in terms of the principal stretch $\lambda := \frac{r}{r_0}$ to obtain $\mathbf{F} = \text{diag}(\lambda^{-2}, \lambda, \lambda)$. A well-known result in continuum mechanics is that the deformation gradient can be decomposed into a product of an orthogonal tensor $\mathbf{R}$ and a symmetric tensor [1]. This is valuable because the orthogonal tensor corresponds to rigid body rotation and hence does not contribute to stress. The decomposition can be carried out in either direction:

$$\begin{aligned} \mathbf{R}_C\mathbf{U} = \mathbf{F} = \mathbf{V}\mathbf{R}_B, \\ \mathbf{V} = \mathbf{R}_C\mathbf{U}\mathbf{R}_B^T. \end{aligned} \tag{46}$$

where $\mathbf{R}_C$ and $\mathbf{R}_B$ represent the orthogonal tensor obtained through each of the above decompositions and $\mathbf{U}$ and $\mathbf{V}$ represent the corresponding symmetric tensors. This leads to two rotation-independent descriptions of the deformation known as the left and right Cauchy-Green deformation tensors, respectively, and given as follows:

$$\begin{aligned} \mathbf{B} &:= \mathbf{F}\mathbf{F}^T = \mathbf{V}^2, \\ \mathbf{C} &:= \mathbf{F}^T\mathbf{F} = \mathbf{U}^2. \end{aligned} \tag{47}$$

2.6.2 Stress-Strain Constitutive Relation for a Spherical, Isotropic, Incompressible, Hyperelastic Shell

In this section, we follow the approach outlined in [1] to obtain the dependence between the Cauchy stress tensor and the strain energy density function for a hyperelastic material.

Ignoring thermal effects for simplicity, the mechanical energy principle requires that the time rate of change of the total mechanical energy for a portion $\mathcal{P}$ of a body $\mathcal{B}$ be equal to the rate of work done by the surface forces (represented by a traction vector $\mathbf{t_n}$) and body forces (represented by a vector $\mathbf{b}$) acting on it [1]. The total mechanical energy of $\mathcal{P}$ consists of its kinetic energy and elastic potential energy which is represented by an energy density function $\Psi(\mathbf{X}, t)$ per unit volume in the reference configuration of $\mathcal{P}$, denoted $\mathcal{P}_0$. The mechanical energy principle can thus be stated mathematically as follows [1]:

$$\frac{d}{dt}\left[\int_{\mathcal{P}} \frac{\rho}{2}\mathbf{v}\cdot\mathbf{v}dv + \int_{\mathcal{P}_0} \Psi dV\right] = \int_{\partial\mathcal{P}} \mathbf{t_n}\cdot\mathbf{v}da + \int_{\mathcal{P}} \mathbf{b}\cdot\mathbf{v}dv, \tag{48}$$

where $\mathbf{v}$ is the velocity and ρ the density. Since $\mathcal{P}$ is not guaranteed to be constant over time, the time derivative cannot immediately be brought into the integral. Instead, a conversion from the current configuration to the reference configuration must be carried out using Equation 44. Denoting $J := \det F$, the left-hand side of the above equation becomes

$$\frac{d}{dt}\left[\int_{\mathcal{P}_0} \frac{\rho J}{2}\mathbf{v}\cdot\mathbf{v}dV + \int_{\mathcal{P}_0} \Psi dV\right] = \int_{\mathcal{P}_0} (\rho J)\mathbf{a}\cdot\mathbf{v}dV + \int_{\mathcal{P}_0} \dot{\Psi} dV. \tag{49}$$

We introduce here several well-known results from continuum mechanics: Cauchy's first and second laws of motion, which are obtained from the conservation of linear and angular momentum, respectively, and Cauchy's stress principle [25]:

$$\operatorname{div}\mathbf{T} + \mathbf{b} = \rho\mathbf{a}, \tag{50}$$

$$\mathbf{T} = \mathbf{T}^T, \tag{51}$$

$$\mathbf{t_n} = \mathbf{T}\mathbf{n}, \tag{52}$$

where $\mathbf{T}$ is the stress tensor, $\mathbf{a}$ is the acceleration vector, and $\mathbf{n}$ is the exterior unit vector normal to $\partial\mathcal{P}$. Applying these to the right-hand side of Equation 48 yields

$$\begin{aligned}\int_{\partial\mathcal{P}} \mathbf{T}\mathbf{v}\cdot\mathbf{n}da + \int_{\mathcal{P}} \mathbf{b}\cdot\mathbf{v}dv &= \int_{\mathcal{P}} \operatorname{div}(\mathbf{T}\mathbf{v})dv + \int_{\mathcal{P}} \mathbf{b}\cdot\mathbf{v}dv \\ &= \int_{\mathcal{P}} [\operatorname{div}\mathbf{T}\cdot\mathbf{v} + \operatorname{tr}(\mathbf{T}\operatorname{grad}\mathbf{v})]dv + \int_{\mathcal{P}} \mathbf{b}\cdot\mathbf{v}dv \\ &= \int_{\mathcal{P}} (\rho\mathbf{a})\cdot\mathbf{v}dv + \int_{\mathcal{P}} \operatorname{tr}(\mathbf{T}\operatorname{grad}\mathbf{v})dv \\ &= \int_{\mathcal{P}_0} (\rho J)\mathbf{a}\cdot\mathbf{v}dV + \int_{\mathcal{P}_0} J\operatorname{tr}(\mathbf{T}\operatorname{grad}\mathbf{v})dV,\end{aligned} \tag{53}$$

where $\operatorname{grad}\mathbf{v} = \frac{\partial\mathbf{v}}{\partial\mathbf{x}}$ is the velocity gradient tensor. It is usually denoted by $\mathbf{L}$. We note that

$$\begin{aligned}\dot{\mathbf{F}} &= \frac{\partial\mathbf{v}}{\partial\mathbf{X}} \\ &= \frac{\partial\mathbf{v}}{\partial\mathbf{x}}\frac{\partial\mathbf{x}}{\partial\mathbf{X}} \\ &= \mathbf{L}\mathbf{F}, \\ \therefore \mathbf{L} &= \dot{\mathbf{F}}\mathbf{F}^{-1}.\end{aligned} \tag{54}$$

Plugging the results from Equations 49 and 53 back into Equation 48, noting that $\mathcal{P}_0$ was arbitrarily chosen, and that the trace of the product of a symmetric and a skew-symmetric matrix is 0 allows us to conclude that

$$\begin{aligned}\dot{\Psi} &= J\operatorname{tr}(\mathbf{T}\mathbf{L}) \\ &= J(T_{ik}\dot{F}_{km}F^{-1}_{mi}) \\ &= (JT_{ki}F^{-T}_{im})\dot{F}_{km} \\ &= T_{R,km}\dot{F}^{T}_{mk} \\ &= \operatorname{tr}(\mathbf{T}_R\dot{\mathbf{F}}^T) \\ &= \mathbf{T}_R : \dot{\mathbf{F}},\end{aligned} \tag{55}$$

where $\mathbf{T}_R \coloneqq J\mathbf{T}\mathbf{F}^{-T}$ is the first Piola-Kirchhoff stress tensor and : denotes the double dot product between two tensors $\mathbf{A} : \mathbf{B} \coloneqq \operatorname{tr}(\mathbf{A}\mathbf{B}^T)$. A hyperelastic solid is defined as a material whose elastic potential energy is given by the following strain energy density function [1]:

$$\Psi(\mathbf{X}, t) = \Psi(\mathbf{F}(\mathbf{X}, t), \mathbf{X}). \tag{56}$$

Applying the chain rule to take the time derivative of Ψ,

$$\frac{d\Psi}{dt} = \frac{\partial \Psi}{\partial \mathbf{F}} : \dot{\mathbf{F}}. \tag{57}$$

Hence, Equation 55 can be re-expressed as

$$\left[\mathbf{T}_R - \frac{\partial \Psi}{\partial \mathbf{F}}\right] : \dot{\mathbf{F}} = 0, \tag{58}$$

which must apply for all $\dot{\mathbf{F}}$; hence,

$$\mathbf{T}_R = \frac{\partial \Psi}{\partial \mathbf{F}} \Leftrightarrow \mathbf{T} = J^{-1} \frac{\partial \Psi}{\partial \mathbf{F}} \mathbf{F}^T. \tag{59}$$

We require the strain energy Ψ to satisfy the principle of material frame indifference which states that the constitutive laws describing the behavior of a material should be indifferent under any change of frame of reference of the observer, i.e., for any orthogonal tensor $\mathbf{Q}$,

$$\Psi(\mathbf{QF}) = \Psi(\mathbf{F}). \tag{60}$$

Recalling the polar decomposition of $\mathbf{F}$ described in Equation 46, we can select $\mathbf{Q} = \mathbf{R}_C^T$ so that

$$\Psi(\mathbf{F}) = \Psi(\mathbf{U}) = \tilde{\Psi}(\mathbf{C}). \tag{61}$$

An isotropic material satisfies the property that a deformation following any rigid body rotation $\mathbf{P}$ results in a similar state of strain, i.e.,

$$\Psi(\mathbf{FP}) = \Psi(\mathbf{F}) \Rightarrow \tilde{\Psi}((\mathbf{FP})^T(\mathbf{FP})) = \tilde{\Psi}(\mathbf{P}^T\mathbf{CP}) = \tilde{\Psi}(\mathbf{C}). \tag{62}$$

Again, letting $\mathbf{P} = \mathbf{R}_C^T$ from Equation 46 gives

$$\tilde{\Psi}(\mathbf{B}) = \tilde{\Psi}(\mathbf{C}). \tag{63}$$

Plugging Equations 61 and 63 into Equation 59 gives

$$\begin{aligned} \mathbf{T} &= J^{-1} \frac{\partial \Psi}{\partial \mathbf{B}} \frac{\partial \mathbf{B}}{\partial \mathbf{F}} \mathbf{F}^T \\ &= 2J^{-1} \frac{\partial \Psi}{\partial \mathbf{B}} \mathbf{B}. \end{aligned} \tag{64}$$

In general, $\mathbf{B}$ and $\mathbf{C}$ have distinct values, although they have the same invariants (which are by definition scalar-valued functions $f(\mathbf{B})$ such that for any orthogonal $\mathbf{Q}$, $f(\mathbf{QBQ}^T) = f(\mathbf{B})$). Equations 61 and 63, obtained by combining the principle of material frame indifference and isotropic requirements, allow us to conclude that the strain energy for a hyperelastic, isotropic material must be dependent only on the invariants of the left or right Cauchy-Green deformation tensors (denoted I_1, I_2, I_3). Reusing Ψ to represent the strain energy density function,

$$\Psi = \Psi(I_1, I_2, I_3). \tag{65}$$

An example of a set of such invariants is

$$\begin{aligned} I_1 &= \mathrm{tr}(\mathbf{B}), \\ I_2 &= \mathrm{tr}(\mathbf{B}^{-1}), \\ I_3 &= \det(\mathbf{F}). \end{aligned} \tag{66}$$

An object is incompressible if $\det \mathbf{F} - 1 = 0$; this imposes a constraint such that the total Cauchy stress tensor can only be determined by $\mathbf{F}$ up to an arbitrary stress [1]:

$$\mathbf{T} = -P\mathbf{I} + \mathbf{T}_E(\mathbf{F}), \tag{67}$$

where $\mathbf{I}$ is the identity tensor and $\mathbf{T}_E$ is the elastic response of the material which has the form given in Equation 64, except that incompressibility implies that $J^{-1} = 1$ and $\Psi = \Psi(I_1, I_2)$. Applying the chain rule,

$$\begin{aligned} \mathbf{T}_E(\mathbf{F}) &= 2\frac{\partial \Psi}{\partial \mathbf{B}}\mathbf{B} \\ &= 2\left(\frac{\partial \Psi}{\partial I_1}\frac{\partial I_1}{\partial \mathbf{B}} + \frac{\partial \Psi}{\partial I_2}\frac{\partial I_2}{\partial \mathbf{B}}\right)\mathbf{B} \\ &= 2\left(\frac{\partial \Psi}{\partial I_1}\mathbf{B} + \frac{\partial \Psi}{\partial I_2}\mathbf{B}^{-1}\right). \end{aligned} \tag{68}$$

Hence,

$$\mathbf{T} = -P\mathbf{I} + 2\left(\frac{\partial \Psi}{\partial I_1}\mathbf{B} + \frac{\partial \Psi}{\partial I_2}\mathbf{B}^{-1}\right). \tag{69}$$

Instead of determining P directly, note that $\mathbf{T}$ can be broken down into hydrostatic stress and deviatoric stresses. Hence, by extracting the hydrostatic portions of $\mathbf{B}$ and $\mathbf{B}^{-1}$ (leaving these terms with only the deviatoric portions) and grouping it

together with $-P\mathbf{I}$ to form the total hydrostatic stress $-p = \frac{\text{tr}(\mathbf{T})}{3}$, and recalling that $\text{tr}(\mathbf{B}) = I_1$, $\text{tr}(\mathbf{B}^{-1}) = I_2$ [15],

$$\mathbf{T} = -p\mathbf{I} + 2\left[\frac{\partial \Psi}{\partial I_1}\left(\mathbf{B} - \frac{I_1}{3}\right) + \frac{\partial \Psi}{\partial I_2}\left(\mathbf{B}^{-1} - \frac{I_2}{3}\right)\right]. \tag{70}$$

For our spherical, isotropic, incompressible, hyperelastic shell, the left Cauchy-Green deformation tensor (in spherical coordinates) is

$$\mathbf{B}_S^e = \begin{bmatrix} \lambda^{-4} & 0 & 0 \\ 0 & \lambda^2 & 0 \\ 0 & 0 & \lambda^2 \end{bmatrix}. \tag{71}$$

which gives

$$\begin{aligned} I_1 &= \lambda^{-4} + 2\lambda^2 \\ I_2 &= \lambda^4 + 2\lambda^{-2}. \end{aligned} \tag{72}$$

Since I_1 and I_2 depend only on the principal stretch λ, it follows that the strain energy density function can be expressed as $\Psi = \Psi(\lambda)$, and

$$\begin{aligned} \frac{d\Psi}{d\lambda} &= \frac{\partial \Psi}{\partial I_1}\frac{dI_1}{d\lambda} + \frac{\partial \Psi}{\partial I_2}\frac{dI_2}{d\lambda} \\ \Rightarrow \frac{\partial \Psi}{\partial I_1} &= \frac{\lambda^5}{4(\lambda^6 - 1)}\frac{d\Psi}{d\lambda} - \lambda^2\frac{\partial \Psi}{\partial I_2}. \end{aligned} \tag{73}$$

Evaluating Equation 70 for the radial term and plugging in Equation 73 gives the final form of the radial term of the stress tensor:

$$\begin{aligned} T_{rr,S}^e &= -p - \frac{4}{3}\frac{\lambda^6 - 1}{\lambda^4}\frac{\partial \Psi}{\partial I_1} - \frac{4}{3}\frac{\lambda^6 - 1}{\lambda^2}\frac{\partial \Psi}{\partial I_2} \\ &= -p - \frac{4}{3}\frac{\lambda^6 - 1}{\lambda^4}\left[\frac{\lambda^5}{4(\lambda^6 - 1)}\frac{d\Psi}{d\lambda} - \lambda^2\frac{\partial \Psi}{\partial I_2}\right] - \frac{4}{3}\frac{\lambda^6 - 1}{\lambda^2}\frac{\partial \Psi}{\partial I_2} \\ &= -p - \frac{\lambda}{3}\frac{d\Psi}{d\lambda}, \end{aligned} \tag{74}$$

where the pressure $p = -\frac{\mathbf{T}_S^e}{3}$ arises from the incompressibility constraint. Denoting $\delta^3 = a^3 - a_0^3$ as the change in volume encompassed by the shell as it changes in radius, we note that due to incompressibility and conservation of mass,

$$\begin{aligned} r^3 - a^3 = r_0^3 - a_0^3 \Rightarrow r^3 &= r_0^3 + \delta^3 \\ \Rightarrow \frac{r_0^3}{r^3} &= 1 - \frac{\delta^3}{r^3} \\ \Rightarrow \lambda &= \left(1 - \frac{\delta^3}{r^3}\right)^{-\frac{1}{3}} \\ \Rightarrow \frac{d\lambda}{dr} &= \frac{\lambda - \lambda^4}{r}. \end{aligned} \tag{75}$$

Plugging Equations 74 and 75 into Equation 27 gives

$$\mathcal{S} = \int_{\frac{a}{a_0}}^{\frac{b}{b_0}} \frac{\Psi'(\lambda)}{\lambda^3 - 1} d\lambda. \tag{76}$$

2.6.3 The Mooney-Rivlin Strain Energy Density Function

The Mooney-Rivlin strain energy density function is used to estimate the strain energy and its derivation is presented as follows [21]. Consider a cylindrical element of volume with unit height and diameter in a hyperelastic material that is (i) homogeneous, (ii) memoryless, (iii) isotropic, and (iv) incompressible, with the property that (v) the traction arising from simple shear in any isotropic plane is proportional to the shear. It is deformed in two steps, a stretch-squeeze in its length dimension of magnitude λ_1 and a shear in the plane normal to the stretch giving rise to principal stretches λ_2 and λ_3 (Fig. 2).

The work done in the first step is thus some function of λ_1:

$$\Psi_1 = \psi(\lambda_1). \tag{77}$$

Since the volume element after the stretch-squeeze has diameter $\frac{1}{\sqrt{\lambda_1}}$, to produce the final principal stretches will require the second stretch to have magnitudes $\lambda_2\sqrt{\lambda_1}$ and $\lambda_3\sqrt{\lambda_1}$. Hence, the shear is

$$\gamma = \sqrt{\lambda_1}(\lambda_2 - \lambda_3). \tag{78}$$

By requirement (v) specified above, the work done per unit volume in the second deformation is

$$\Psi_2 = \lambda_1(\lambda_2 - \lambda_3)^2\phi(\lambda_1). \tag{79}$$

Adding the above and keeping in mind the incompressibility requirement $\lambda_1\lambda_2\lambda_3 = 1$, the total work done can be expressed as